

# Simulation of Square Wave Voltammetry: Quasi-Reversible Electrode Processes

Benjamin A. Brookes and Richard G. Compton\*

Physical and Theoretical Chemistry Laboratory, Oxford University, South Parks Road, Oxford, OX1 3QZ, United Kingdom

Received: May 6, 1999; In Final Form: August 18, 1999

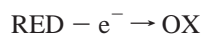
Simulations, based on the backward implicit method, for the square wave voltammetry (SWV) experiment are reported for the general case of quasi-reversible Butler–Volmer kinetics and a finite diffusion layer thickness. In the limiting cases of fast electrode kinetics, or semi-infinite diffusion, the results are in excellent agreement with independent calculations confirming the validity of the approach and its implementation. Under the previously unexplored conditions of finite diffusion, the effect of the diffusion layer thickness on the peak characteristics—width, height, and voltage—are identified and quantified, so providing a quantitative basis for the use of SWV at hydrodynamic electrodes for the determination of electrochemical kinetic parameters.

## 1. Introduction

Square wave voltammetry (SWV) is a highly attractive and especially sensitive method for the study of diverse electrochemical processes. The technique involves the application of the general potential waveform defined in Figure 1 and the measurement of the currents  $I(1)$  and  $I(2)$  in each cycle of the waveform at the points shown. The current difference,

$$\Delta I = I(1) - I(2)$$

is highly discriminating against background currents and the variation of  $\Delta I$  with potential typically gives rise to peak-shaped voltammograms, which are highly sensitive to the electrode kinetics. SWV for redox couples with electrochemically irreversible or quasi-reversible kinetics has been modeled by approximate analytical theory for the case of semi-infinite diffusion. In particular, for the case<sup>1–3</sup> of



an integral equation approach was used to estimate the dimensionless current, defined as:

$$\Delta I_{\text{DL}} = \Delta I \frac{\sqrt{\pi\nu}}{FA\sqrt{D_{\text{RED}}[\text{RED}]_{\text{bulk}}}}$$

where  $\nu$  is the square wave period,  $A$  the electrode surface area,  $D_{\text{RED}}$  the RED species diffusion coefficient, and  $[\text{RED}]_{\text{bulk}}$  the bulk concentration of the RED species, and assuming absence of the OX species in solution. In this approach, the continuous function  $\Delta I_{\text{DL}}$  was replaced by

$$b_m = \frac{\frac{\pi}{1+\epsilon} \sqrt{\frac{l}{2}} - \sum_{i=1}^{m-1} b_i s'_j}{1 + \sqrt{\frac{l\pi}{2\nu} \left( \frac{1}{\kappa\epsilon^{-\alpha}(1+\epsilon)} \right)}} \quad (1)$$

where  $l$  is the number of subintervals per half-period,  $b_m$  is the

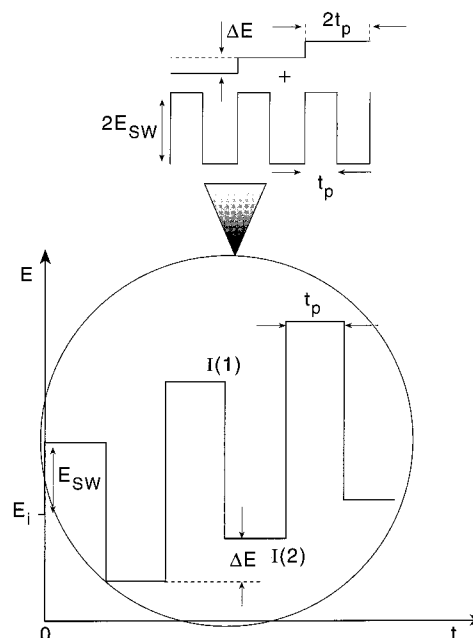


**Figure 1.** Schematic diagram defining the square wave voltammetry experiment where  $\Delta E$  is the step voltage,  $E_{\text{sw}}$  is the square wave voltage,  $E_i$  the initial voltage, and  $t_p$  the duration of a pulse.

approximation to  $I_{\text{DL}}(t)$  at  $t = mv/2l$ ,  $S'_j = \sqrt{j} - \sqrt{j-1}$ ,  $j = m - i + 1$ ,  $\epsilon = \exp[F(E - E^\circ)/RT]$ ,  $\alpha$  is the transfer coefficient (see below),  $E$  is the potential of the square-wave scan, and  $E^\circ$  the formal potential of the redox couple.

In this paper, we develop a complementary finite difference simulation approach, which will be seen to be significantly more computationally efficient than the integral equation method. More importantly, the former is readily adaptable to predict the effects of finite diffusion layer thickness on the observed voltammetry. This provides a rigorous basis for the quantitative development of SWV at hydrodynamic electrodes such as rotating disk electrodes, an attractive and sensitive means for the determination of electrode kinetic parameters. The influence of variable diffusion layer thicknesses on the SWV experiment applied to electrochemically quasi-reversible systems is discussed.

\* To whom correspondence should be sent.

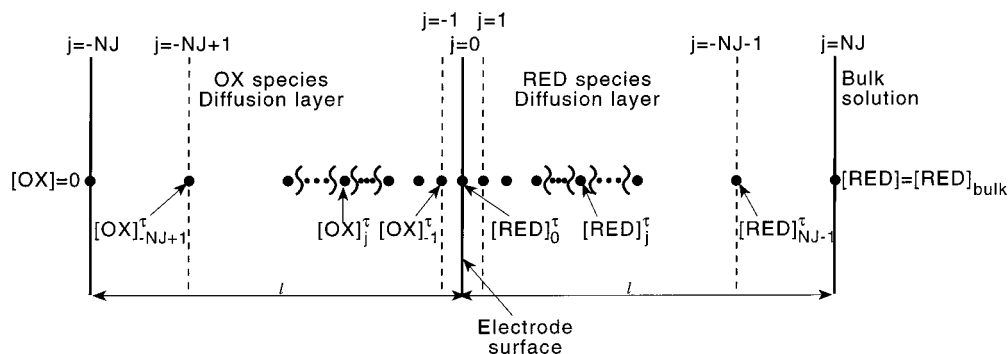


**Figure 2.** Schematic diagram showing the spatial node distribution in the back-to-back grid where  $j$  denotes the spatial element and  $\tau$  the temporal element.

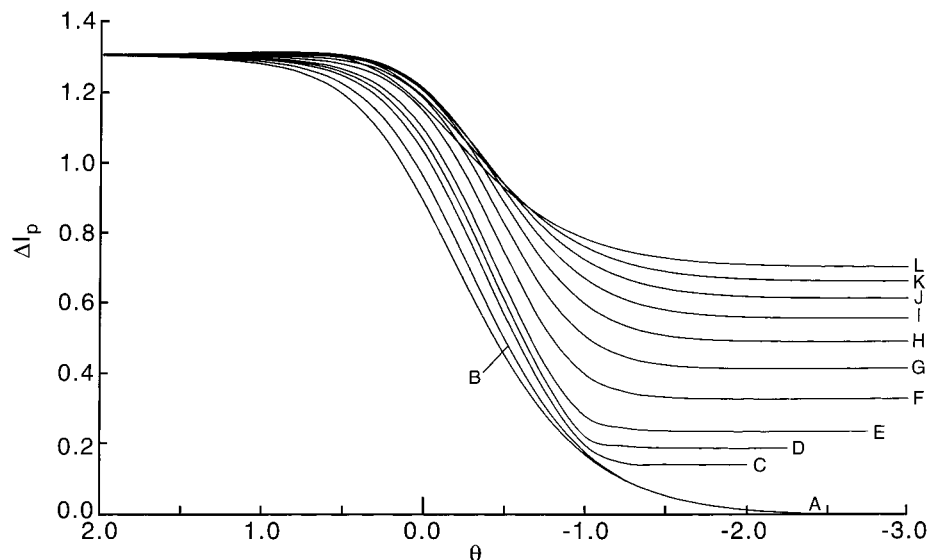
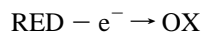


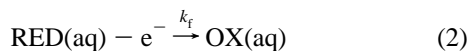
**Figure 3.** Graphs showing the variation of dimensionless peak current,  $\Delta I_p$ , as a function of  $\theta$ , for several values of  $\beta$ : (A–L)  $\beta = 0.0, 0.1, 0.2, 0.25, 0.3, 0.4, 0.5, 0.6, 0.7, 0.8, 0.9, 1.0$ .

## 2. Theory

We consider the simple redox reaction,



at the surface of a uniformly accessible electrode. The couple has forward and backward rate constants:



where the rate constants  $k_f$  and  $k_b$  are assumed to be governed by Butler–Volmer kinetics and are exponentially related to the parameter  $F(E - E^\circ)/RT$ , such that

$$k_f = k_0 \exp\left[\frac{\beta F}{RT}(E - E^\circ)\right] \quad (4)$$

$$k_b = k_0 \exp\left[\frac{-\alpha F}{RT}(E - E^\circ)\right] \quad (5)$$

where  $\alpha$  and  $\beta$  are a transfer coefficients, and  $\alpha + \beta = 1$ .

Mass transport equations for both species in solution are given by Fick's second law:

$$\frac{\partial[\text{RED}]}{\partial t} = D_{\text{RED}} \frac{\partial^2[\text{RED}]}{\partial y^2} \quad (6)$$

$$\frac{\partial[\text{OX}]}{\partial t} = D_{\text{OX}} \frac{\partial^2[\text{OX}]}{\partial y^2} \quad (7)$$

where  $D$  denotes the appropriate diffusion coefficient.

The concentration of the reduced species tends to its bulk value far from the electrode, while that of the oxidized species approaches zero. Hence the following boundary conditions can be formulated:

$$[\text{RED}]_{y=l} = [\text{RED}]_{\text{bulk}}$$

$$[\text{OX}]_{y=l} = 0$$

where  $l$  is the length of the diffusion layer of the electrode.

At the electrode surface the flux of OX and RED species is conserved, and its magnitude depends on diffusion as well as the rate of kinetic interconversion. These considerations generate further boundary conditions.

$$D_{\text{RED}} \frac{\partial[\text{RED}]}{\partial y}\bigg|_{y=0} = -D_{\text{OX}} \frac{\partial[\text{OX}]}{\partial y}\bigg|_{y=0} \quad (8)$$

$$D_{\text{RED}} \frac{\partial[\text{RED}]}{\partial y}\bigg|_{y=0} = k_f[\text{RED}]_{y=0} - k_b[\text{OX}]_{y=0} \quad (9)$$

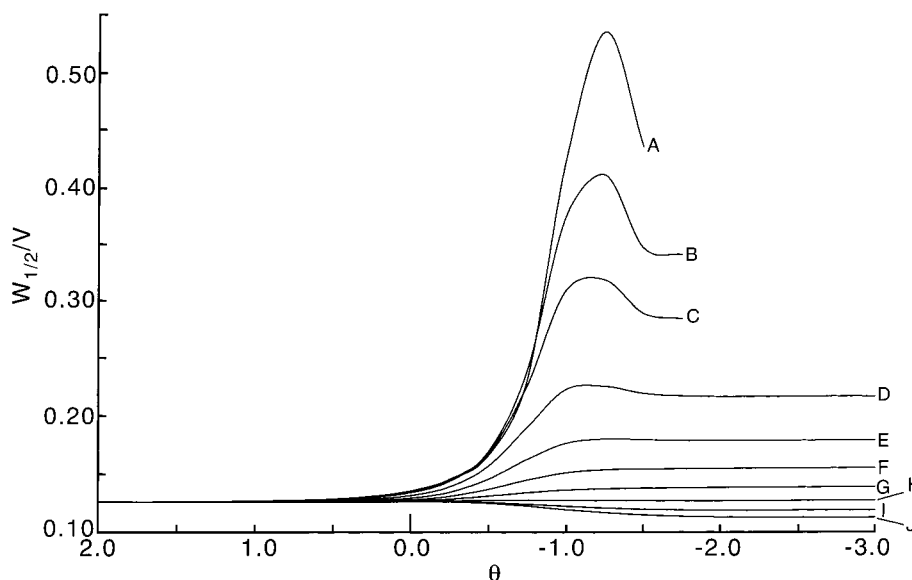


**Figure 4.** Peak width,  $W_{1/2}$ , as a function of  $\theta$ , for several values of  $\beta$ : (A–L)  $\beta = 0.0, 0.1, 0.2, 0.25, 0.3, 0.4, 0.5, 0.6, 0.7, 0.8, 0.9, 1.0$ .

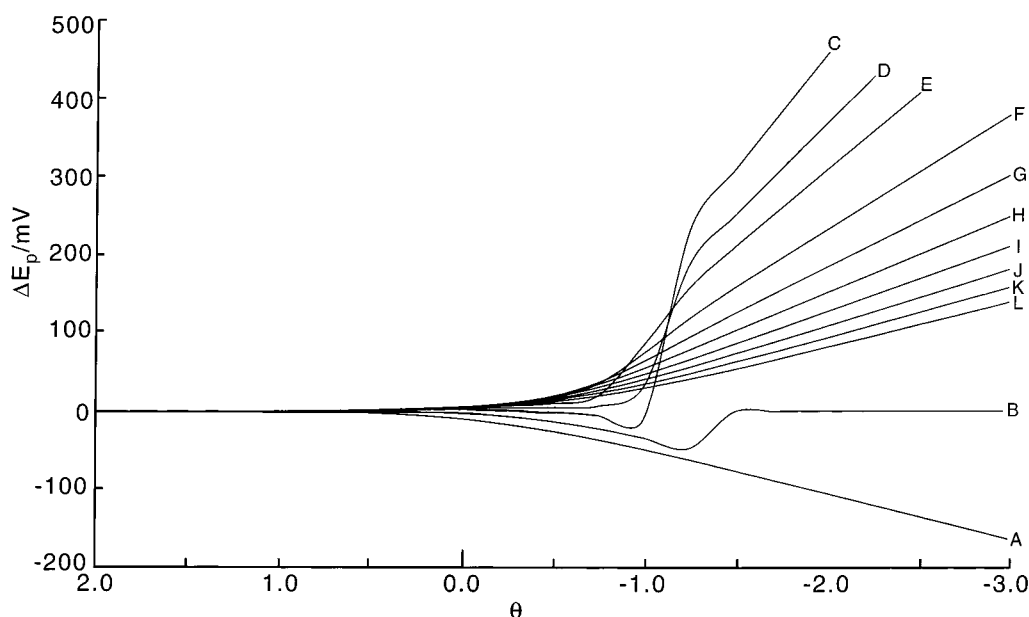


**Figure 5.** Peak shift,  $\Delta E_p$ , as a function of  $\theta$ , for several values of  $\beta$ : (A–J)  $\beta = 0.2, 0.25, 0.3, 0.4, 0.5, 0.6, 0.7, 0.8, 0.9, 1.0$ .

To solve mass transport eqs 6 and 7 for the SWV experiment, under the above boundary conditions, we use the backward implicit method<sup>4–6</sup> as documented in our preceding paper<sup>7</sup> for reversible electrode kinetics. The simulation makes use of a back-to-back grid,<sup>8–10</sup> where the positive  $y$  coordinate is used to simulate the RED species and the negative  $y$  coordinate to represent the OX species. The electrode is placed at  $y = 0$ . The grid is shown in Figure 2. The mathematics developed below lead to the concentrations of both OX and RED species at the electrode surface being handled implicitly. Time and space coordinate transformations<sup>7</sup> are employed in the simulation. In particular, the temporal transformation is a “Cottrellian time grid”<sup>11</sup> where there are two distorted time scales, one for forward pulses,

$$\tau_f = \sqrt{\frac{t_p}{t - b}} \quad (10)$$

and another for backward pulses,

$$\tau_b = \sqrt{\frac{t_p}{t - t_p - b}} - \sqrt{\frac{t_p}{t - b}} \quad (11)$$

In these equations,  $\tau$  is the transformed time coordinate,  $t_p$  the pulse length is seconds, and  $b$  is a small time offset used to optimize the simulations; in practice, values of  $b$  equal to  $t_p/500$  were optimal. For the spatial transformation, a hyperbolic function is employed such that

$$\psi = \tanh\left(\frac{ya}{l}\right) \quad (12)$$

where  $\psi$  is the transformed distance,  $y$  is the real distance,  $a$  is scaling parameter (typically chosen to be 20), and  $l$  is the semi-infinite diffusion layer thickness (200  $\mu\text{m}$ ).

The finite-difference form of eq 9 is

$$D_{\text{RED}} \left( \frac{\partial \psi}{\partial y} \right)_{y=0} \left( \frac{[\text{RED}]_1 - [\text{RED}]_0}{\Delta \psi} \right) = k_f [\text{RED}]_0 - k_b [\text{OX}]_0 \quad (13)$$

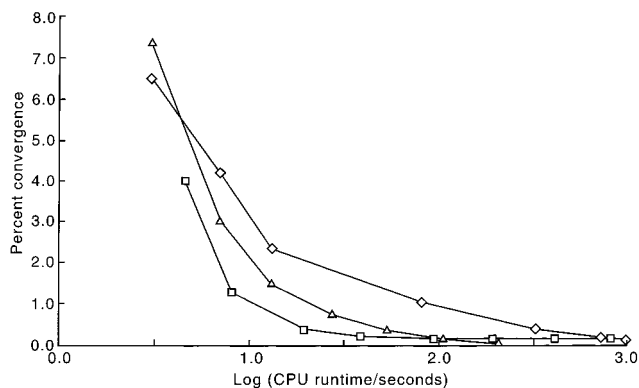


**Figure 6.** Graph showing the variations in percentage convergence of dimensionless peak current,  $\Delta I_p$ , for the solution to eq 1 ( $\diamond$ ), for the simulation converged in  $NJ$ , with  $NL$  held constant ( $\square$ ), and for the simulation converged in  $NL$  with  $NJ$  held constant ( $\triangle$ ), as a function of  $\log(\text{CPU runtime/seconds})$ .

where  $\Delta\psi = \tanh(a)/NJ$ .

Conversion of eq 8 into finite-difference form gives

$$D_{\text{RED}}([RED]_1 - [RED]_0) + D_{\text{OX}}([OX]_{-1} - [OX]_0) = 0 \quad (14)$$

Substitution of  $[OX]_0$  or  $[RED]_0$  from eq 14 into eq 9 gives explicit solutions for either  $[RED]_0$  or  $[OX]_0$  in terms of  $[RED]_1$  and  $[OX]_{-1}$ .<sup>10</sup>

$$[RED]_0 = k_{a1}[RED]_1 + k_{a2}[OX]_{-1} \quad (15)$$

and

$$[OX]_0 = k_{b1}[OX]_{-1} + k_{b2}[RED]_1 \quad (16)$$

where

$$\begin{aligned} k_{a1} &= \frac{k_b D_{\text{REL}} + \phi_{\text{RED}}}{k_f + k_b D_{\text{REL}} + \phi_{\text{RED}}} \\ k_{a2} &= \frac{k_b}{k_f + k_b D_{\text{REL}} + \phi_{\text{RED}}} \\ k_{b1} &= \frac{\frac{k_f}{D_{\text{REL}}} + \phi_{\text{OX}}}{\frac{k_f}{D_{\text{REL}}} + k_b + \phi_{\text{OX}}} \\ k_{b2} &= \frac{k_f}{\frac{k_f}{D_{\text{REL}}} + k_b + \phi_{\text{OX}}} \\ D_{\text{REL}} &= \frac{D_{\text{RED}}}{D_{\text{OX}}}, \quad \phi_{\text{OX}} = \frac{a D_{\text{OX}}}{l \Delta\psi}, \quad \phi_{\text{RED}} = \frac{a D_{\text{RED}}}{l \Delta\psi} \end{aligned}$$

It is possible to formulate a full set of finite-difference equations from mass transport eqs 6 and 7. For RED species in solution ( $j = NJ - 2$  to  $2$ ):

$$\begin{aligned} [RED]_j^{\tau-1} &= -\lambda^{\text{RED}}(1 - \psi_j^2 + \psi_j \Delta\psi)[RED]_{j-1}^{\tau} \\ &+ (1 + 2\lambda^{\text{RED}}(1 - \psi_j^2))[RED]_j^{\tau} \\ &- \lambda^{\text{RED}}(1 - \psi_j^2 - \psi_j \Delta\psi)[RED]_{j+1}^{\tau} \end{aligned} \quad (17)$$

For OX species in solution ( $j = -NJ + 2$  to  $-2$ ):

$$\begin{aligned} [OX]_j^{\tau-1} &= -\lambda^{\text{OX}}((1 - \psi_j^2) + \psi_j \Delta\psi)[OX]_{j-1}^{\tau} \\ &+ (1 + 2\lambda^{\text{OX}}(1 - \psi_j^2))[OX]_j^{\tau} \\ &- \lambda^{\text{OX}}((1 - \psi_j^2) - \psi_j \Delta\psi)[OX]_{j+1}^{\tau} \end{aligned} \quad (18)$$

The introduction of the following boundary conditions allows us to generate the finite-difference equations at the electrode surface and the edge of the diffusion layer.

$$t = 0$$

$$[OX]_j = 0 \quad \text{for } j = -1, -2, -3, \dots, -NJ$$

$$[RED]_j = [RED]_{\text{bulk}} \quad \text{for } j = 0, 1, 2, 3, \dots, NJ$$

$$t > 0; \quad y = l \quad (j = NJ)$$

$$[RED]_{NJ} = [RED]_{\text{bulk}}$$

$$t > 0; \quad y = l \quad (j = -NJ)$$

$$[OX]_j = 0$$

At the electrode surface,

$$\begin{aligned} [OX]_{-1}^{\tau-1} &= -\lambda^{\text{OX}}(1 - \psi_j^2 + \psi_j \Delta\psi)[OX]_{-1}^{\tau} \\ &+ (1 + 2\lambda^{\text{OX}}(1 - \psi_j^2) - \lambda^{\text{OX}}(1 - \psi_j^2 - \psi_j \Delta\psi)k_{b1})[OX]_{-1}^{\tau} \\ &- \lambda^{\text{OX}}(1 - \psi_j^2 + \psi_j \Delta\psi)k_{b2}[RED]_1^{\tau} \end{aligned} \quad (19)$$

and

$$\begin{aligned} [RED]_1^{\tau-1} &= -\lambda^{\text{RED}}(1 - \psi_j^2 + \psi_j \Delta\psi)k_{a2}[OX]_{-1}^{\tau} \\ &+ (1 + 2\lambda^{\text{RED}}(1 - \psi_j^2) - \lambda^{\text{RED}}(1 - \psi_j^2 - \psi_j \Delta\psi)k_{a1})[RED]_1^{\tau} \\ &- \lambda^{\text{RED}}(1 - \psi_j^2 + \psi_j \Delta\psi)[RED]_2^{\tau} \end{aligned} \quad (20)$$

At the bulk solution boundary,  $j = NJ - 1$  for RED species and  $j = -NJ + 1$  for OX species:

$$\begin{aligned} [RED]_{NJ-1}^{\tau-1} + \lambda^{\text{RED}}[RED]_{\text{bulk}} &= \\ &- \lambda^{\text{RED}}(1 - \psi_j^2 + \psi_j \Delta\psi)[RED]_{NJ-2}^{\tau} \\ &+ (1 - \lambda^{\text{RED}}(1 - \psi_j^2))[RED]_{NJ-1}^{\tau} \end{aligned} \quad (21)$$

and

$$\begin{aligned} [OX]_{-NJ+1}^{\tau-1} &= (1 - 2\lambda^{\text{OX}}(1 - \psi_j^2))[OX]_{-NJ+1}^{\tau} \\ &- \lambda^{\text{OX}}(1 - \psi_j^2 + \psi_j \Delta\psi)[OX]_{-NJ+2}^{\tau} \end{aligned} \quad (22)$$

where

$$\lambda^i = \frac{-D_i \Delta\tau(1 - \psi_j^2)\left(\frac{a}{l}\right)^2}{(\Delta\psi)^2 \left(\frac{\partial\tau}{\partial t}\right)}$$

and  $i = \text{RED or OX}$ .

For the backward pulse, there is no explicit form of  $t$  in terms of  $\tau_b$ . It is therefore necessary to evaluate the derivative  $\partial\tau/\partial t$ , by use of the Adam's variable-order variable-step method.<sup>12</sup>

The relevant equations may be grouped together to form a tridiagonal matrix, which is solvable using the Thomas algorithm.<sup>13,14</sup> The currents  $I(1)$  and  $I(2)$  can then be calculated at the end of each half cycle as

$$I = nFAD_{\text{RED}} \left( \frac{\partial[RED]}{\partial\psi} \right)_{y=0} \left( \frac{\partial\psi}{\partial y} \right)_{y=0}$$

In finite-difference form this is

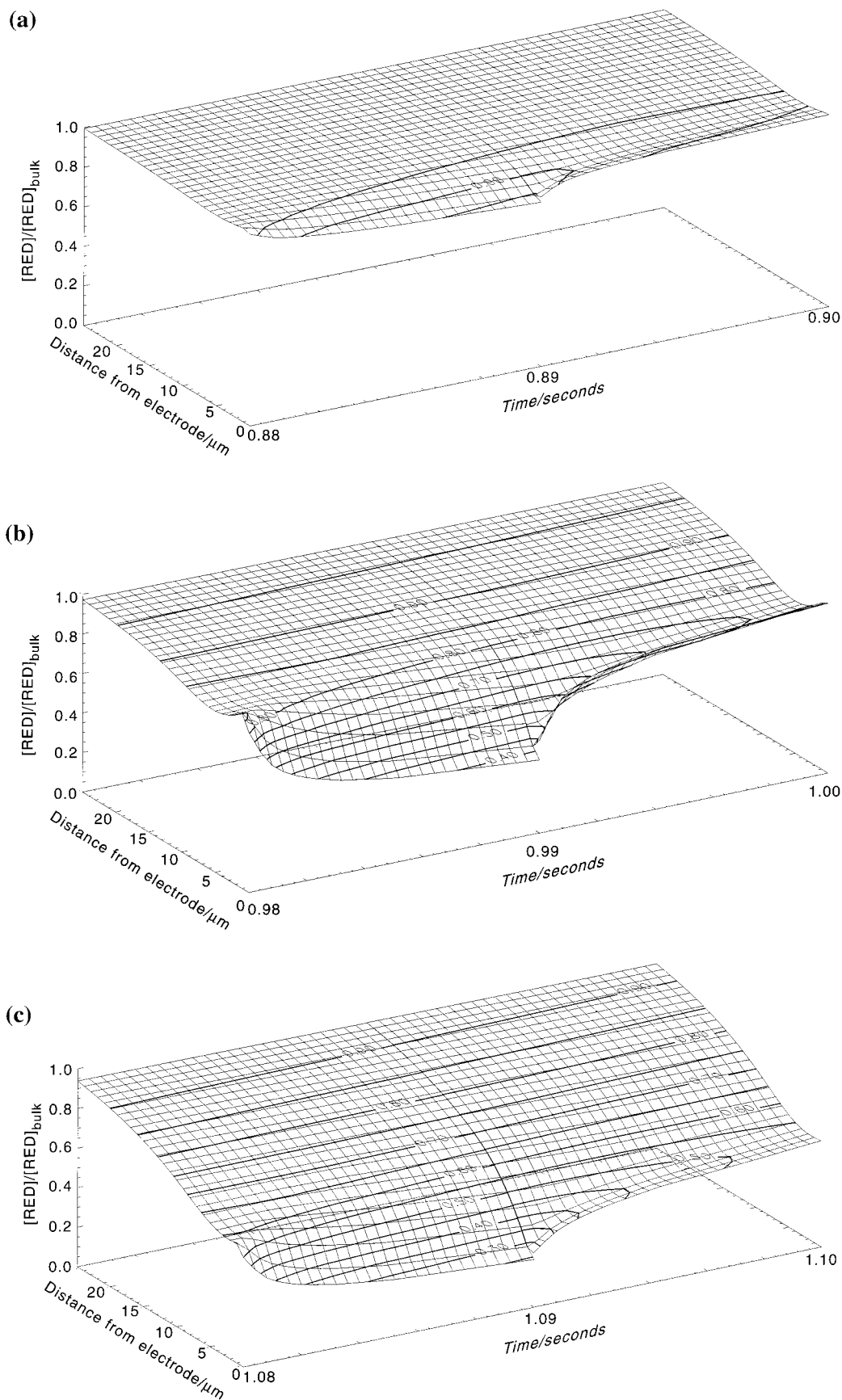


**Figure 7.** Concentration profiles for the RED species during (a) the 45th cycle with  $E = -10$  mV at time 0.88–0.89 s from the start of the experiment and  $E = -110$  mV at 0.89–0.90 s, (b) the 50th cycle with  $E = 40$  mV (0.98–0.99 s) and  $E = -60$  mV (0.99–1.00 s), (c) the 55th cycle with  $E = 90$  mV (1.08–1.09 s) and  $E = -10$  mV (1.09–1.10 s). The full set of parameters used in the simulations is given in the text.

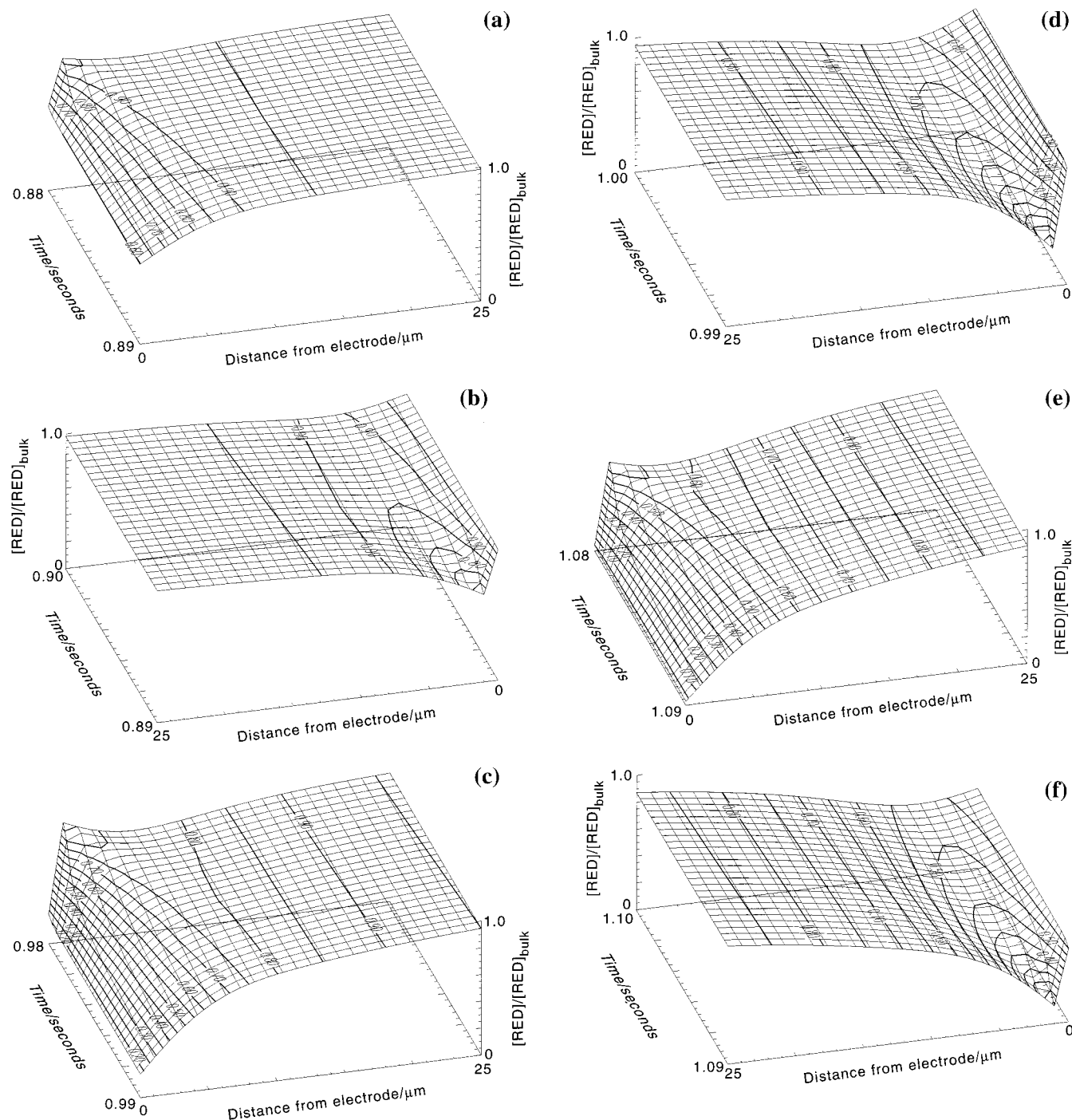


**Figure 8.** Concentration profiles for the RED species during (a) the forward pulse of the 45th cycle with  $E = -10$  mV, (b) the backward pulse of the 45th cycle with  $E = -110$  mV, (c) the forward pulse of the 50th cycle with  $E = 40$  mV, (d) the backward pulse of the 50th cycle with  $E = -60$  mV, (e) the forward pulse of the 55th cycle with  $E = 90$  mV, and (f) the backward pulse of the 55th cycle with  $E = -10$  mV. The simulation is calculated for a reversible electrode process.

$$I = nFAD_{\text{RED}} \left( \frac{a}{l} \right) \left( \frac{[\text{RED}]_1^r - [\text{RED}]_0^r}{\Delta\psi} \right)$$

or alternatively, in dimensionless form,

$$\Delta I_{\text{DL}} = \Delta I \frac{\sqrt{\pi\nu}}{FA\sqrt{D_{\text{RED}}[\text{RED}]_{\text{bulk}}}}$$

The simulation was compiled using FORTRAN 77, and the numerical calculation of eq 1 using C. Both programs were

executed on a Silicon Graphics Origin 2000 server. Results were analyzed using Excel 5.0 and the concentration profiles drawn using IDL.

### 3. Results and Discussion

We consider first our results obtained under conditions of semi-infinite diffusion where the theory of Osteryoung and co-workers,<sup>15</sup> is applicable. They found that two independent parameters,  $\beta$  and  $\theta$ , where

$$\theta = \log(\kappa\sqrt{\nu}) \quad (23)$$

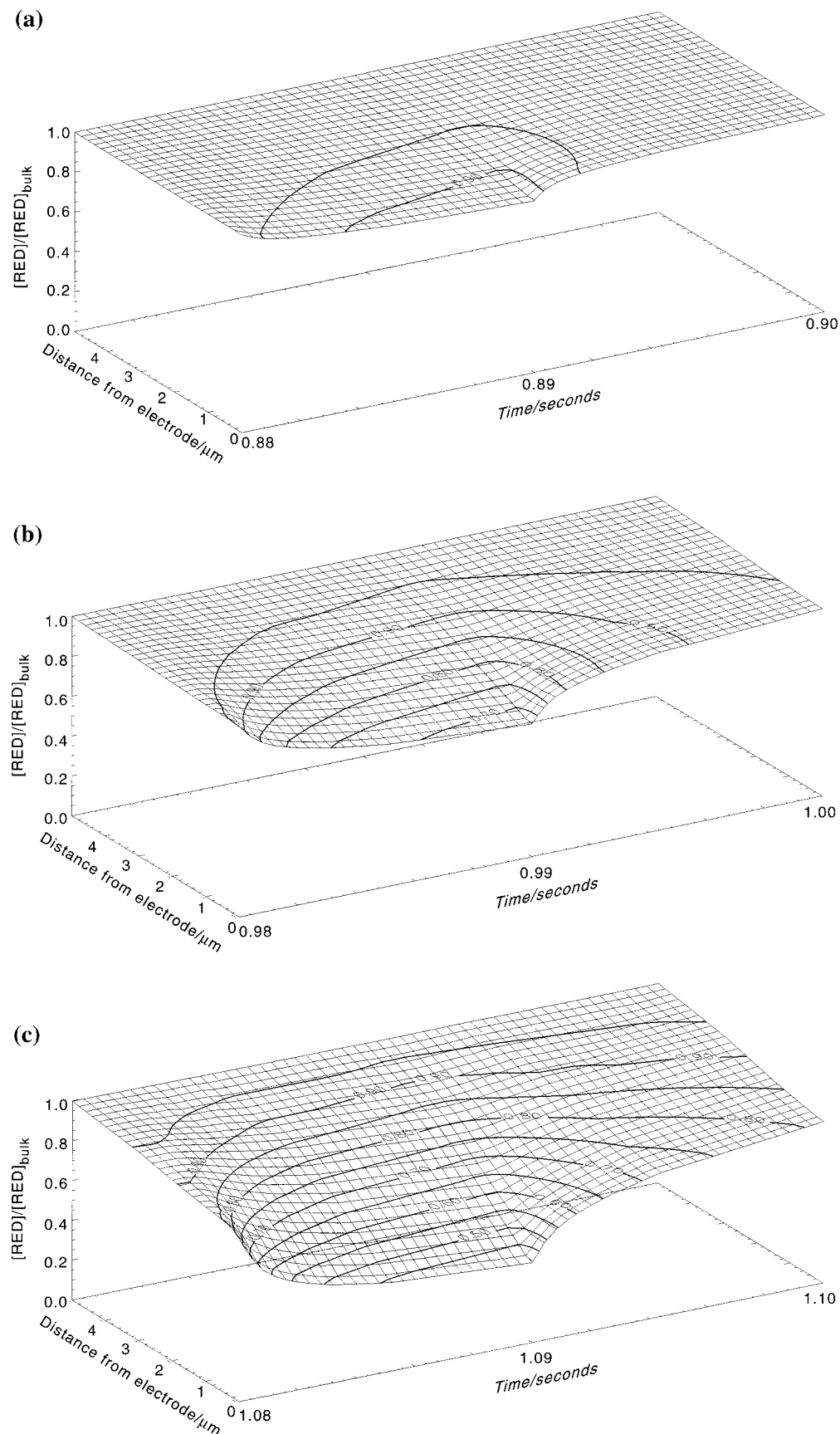


**Figure 9.** Concentration profiles for the RED species during (a) the 45th cycle with  $E = -10$  mV at time 0.88–0.89 s from the start of the experiment and  $E = -110$  mV at 0.89–0.90 s, (b) the 50th cycle with  $E = 40$  mV (0.98–0.99 s) and  $E = -60$  mV (0.99–1.00 s), (c) the 55th cycle with  $E = 90$  mV (1.08–1.09 s) and  $E = -10$  mV (1.09–1.10 s). The simulation is calculated for a quasi-reversible electrode process with diffusion layer thickness of  $5\ \mu\text{m}$ .



and

$$\kappa = \frac{k_0}{(D_{\text{RED}})^{\alpha/2} (D_{\text{OX}})^{\beta/2}}$$

characterize the SWV behavior of the redox couple. These control the three parameters that characterize the voltammogram. These are the dimensionless peak current,  $\Delta I_p$ , the peak width at half-height,  $W_{1/2}$ , and the peak shift,  $\Delta E_p$ , defined as

$$\Delta E_p = E_p - E^{0'}$$

where  $E_p$  is the potential of the current maximum on the square wave voltammogram. Values for  $\Delta I_p$  and  $\Delta E_p$  were deduced from the simulated current data by curve-fitting five values of  $\Delta I$  centered around the peak in the potential–current curve and solving the resulting cubic equation, while those for  $W_{1/2}$  were found by linear interpolation at half the peak height.

Voltammograms were simulated for a range of  $\theta$  values between  $-3.0$  and  $2.0$  and  $\beta$  values between  $0$  and  $1$ . The level of accuracy at which the simulation is run, depends on two parameters, first  $NJ$  specifies the amount of spatial points used in the simulation, and second,  $NL$  specifies the number of temporal simulations that occur in a single pulse, being separated by equal intervals in  $\tau$ . Representative simulations were first fully converged to values of  $NJ = 4000$  and  $NL = 8000$ . Subsequent simulations were run with  $\Delta E_p$ , the most sensitive parameter, converged to  $1\%$  in both  $NL$  and  $NJ$ , for economy of CPU runtime. For comparison, eq 1 was solved, and calculations were run for the identical values of  $\beta$  and  $\theta$  as in the simulations. Accuracy here was dependent only on  $l$ , which was set to  $100$ , representing a convergence in  $\Delta E_p$  of  $0.56\%$ , relative to the value given at  $l = 250$ . Graphs of  $\Delta I_p$ ,  $\Delta E_p$ , and  $W_{1/2}$  for simulated data are shown in Figures 3–5.

Comparison of the data in Figure 3 with the solution of eq 1 showed that the values of  $\Delta I_p$  calculated in the two different ways were simulated to within  $\pm 1.2\%$  over the values of  $\theta$  studied. The percentage difference in the results of  $W_{1/2}$  was smaller and typically in the range  $-0.5$  to  $+0.5\%$ , although for small  $\beta$  values the agreement was to within  $1\%$ . Agreement in  $\Delta E_p$  was typically between  $+0.6$  and  $-0.1$  mV.

To compare the relative computational merits of the simulation approach and the integral equation method, data was collected for  $\Delta I_p$ , as well as the CPU time needed for the calculations, over a range of convergences relative to the fully converged value as explained above. Figure 6 shows an

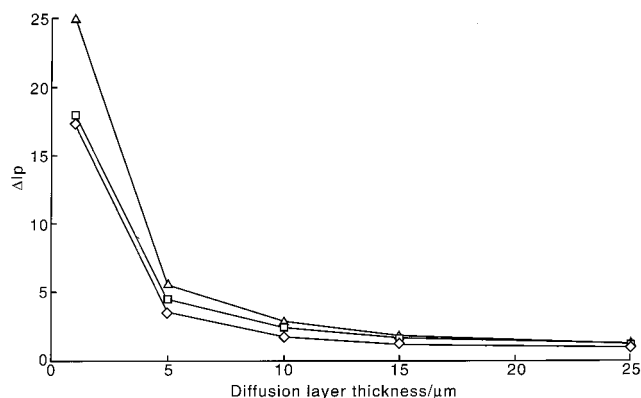


**Figure 10.** Graph showing the variation of dimensionless peak current,  $\Delta I_p$ , as a function of diffusion layer thickness for values of  $k_0$ :  $1.0$  ( $\Delta$ );  $0.1$  ( $\square$ );  $0.01 \text{ cm s}^{-1}$  ( $\diamond$ ). The other simulation parameters were as for Figure 7.

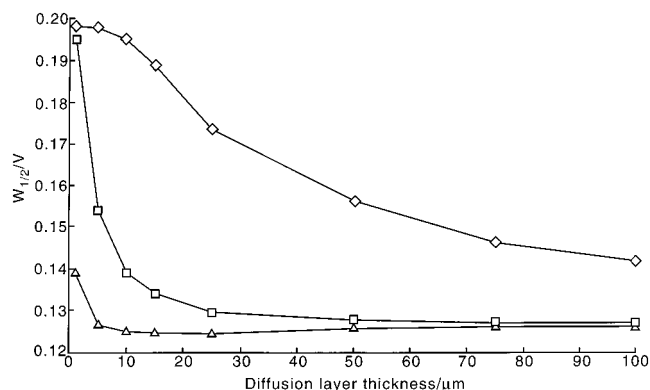


**Figure 11.** Graph showing the variation of peak shift,  $W_{1/2}$ , as a function of diffusion layer thickness, for values of  $k_0$ :  $1.0$  ( $\Delta$ );  $0.1$  ( $\square$ );  $0.01 \text{ cm s}^{-1}$  ( $\diamond$ ). The other simulation parameters were as for Figure 7.

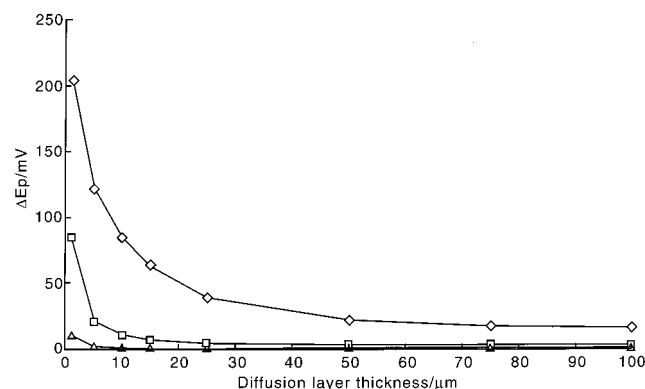


**Figure 12.** Graph showing the variation of peak width,  $\Delta E_p$ , as a function of diffusion layer thickness, for values of  $k_0$ :  $1.0$  ( $\Delta$ );  $0.1$  ( $\square$ );  $0.01 \text{ cm s}^{-1}$  ( $\diamond$ ). The other simulation parameters were as for Figure 7.

efficiency plot of percentage convergence versus  $\log(\text{CPU runtime/seconds})$ . Since the simulation has two variables ( $NJ$  and  $NL$ ) that affect the value of  $\Delta I_p$ , these were altered independently to produce two efficiency curves. The results in Figure 6 show that in the range of CPU time studied, the simulation is more efficient than the numerical method, particularly at modest but useful convergence values. For example, at about  $1\%$  convergence, the numerical solution to eq 1 takes  $81 \text{ s}$ , versus a possible  $10 \text{ s}$  for the simulation, when  $NL$  is held constant. For faster simulations ( $5$ – $100 \text{ s}$ ), increasing  $NJ$  while holding  $NL$  constant gives the best efficiency, while for more accurate simulations ( $100$ – $1000 \text{ s}$ ), altering  $NJ$  while keeping  $NL$  constant gave the best efficiency. We conclude that the simulation approach is an accurate and efficient method for understanding the SWV problem, for quasi-reversible kinetics.

A particular merit of the simulation method is the immediate ability to view concentration profiles close to the electrode surface, as a function of both potential and time. Parts a–c of Figure 7 show a sequence of such profiles for a simulation with the following parameters:  $E_{\text{sw}} = 50 \text{ mV}$ ;  $\Delta E = 10 \text{ mV}$ ;  $f = 50 \text{ Hz}$ ;  $E^{0'} = 0 \text{ V}$ ;  $E_i = -500 \text{ mV}$ ;  $E_f = 500 \text{ mV}$ ;  $\theta = -0.5$  (corresponding to a value of  $k_0$  of  $7.1 \times 10^{-3} \text{ cm s}^{-1}$ );  $\alpha = 0.5$ ;  $l = 200 \mu\text{m}$ , where  $E_i$  and  $E_f$  are the initial and final potentials, respectively. The potential scan therefore involves  $100$  cycles or  $200$  pulses. The figures show the spatial distribution of the RED species at the 45th, 50th, and 55th cycles. Hence, each figure shows the combination of one forward pulse, where the RED species is converted to OX, and



one backward pulse, where OX is converted back to RED. To contrast the case of quasi-reversible kinetics with a couple with fully reversible kinetics,<sup>7</sup> parts a–e of Figure 8 show concentrations for the same experiment, but with  $\theta = +2.0$  (corresponding to a value of  $k_0$  of  $2.2 \text{ cm s}^{-1}$ ). The profiles for each pulse are shown individually for clarity. Considering first the profiles shown in Figure 7, these illustrate that, as the overpotential becomes more positive, there is a net increase of OX species close to the surface of the electrode. However second, noting Figure 7, unlike SWV with a reversible couple, where the instantaneous changes in potential produce an immediate reequilibration of the concentrations of OX and RED species at the electrode surface, with quasi-reversible kinetics, we observe smooth variations in concentrations.

Next, simulations were conducted for diffusion layers of finite value in the range 1–200  $\mu\text{m}$ . Typical profiles are shown in Figure 9, where the data have been calculated using the same parameters as employed above for the case of Figure 7, but with a diffusion layer thickness of 5  $\mu\text{m}$ . Comparison of Figures 9 and 7 shows that for this diffusion layer thickness which, for example, can be readily attained by insonation<sup>16</sup> of the electrode, the concentration profiles have reached the edge of the diffusion layer long before the end of each of the three cycles shown. Consequently, significant hydrodynamic perturbation of the SWV response may be expected. Accordingly, simulations were run, as above, but for  $k_0$  values of 1.0, 0.1, and  $0.01 \text{ cm s}^{-1}$ , using a wide range of diffusion layer thicknesses to calculate the effect on the three parameters,  $\Delta I_p$ ,  $W_{1/2}$ , and  $\Delta E_p$ . The results are shown in Figures 10–12, which show the response to be highly sensitive to both parameters, except where the diffusion layer is sufficiently large that semi-infinite diffusion operates. Implicit in the data is the use of SWV measurements at hydrodynamic electrodes to sensitively probe electrode kinetics.

## Conclusions

The simulation of the SWV experiment for uniformly accessible electrodes is computationally efficient and readily allows both the visualization of concentration profiles during pulse sequences and the inclusion of finite diffusion layer effects. The extension to coupled homogeneous kinetics and microelectrode geometries is envisaged and the subject of current work.

## References and Notes

- (1) Aoki, K.; Tokuda, K.; Matsuda, H.; Osteryoung, J. J. *Electroanal. Chem.* **1986**, 207, 25.
- (2) O'Dea, J. J.; Osteryoung, R. A. *Anal. Chem.* **1981**, 53, 695.
- (3) Nicholson, R.S.; Olmstead, M.L. In *Electrochemistry: Calculations, Simulation and Instrumentation*; Mattson, J. S., Mark, H. B., MacDonald, H. C., Eds.; Marcel Dekker: New York, 1972; Vol. 2.
- (4) Anderson, J.L.; Moldoveanu, S. J. *Electroanal. Chem.* **1984**, 179, 109.
- (5) Laasonen, P. *Acta. Math.* **1949**, 81, 30917.
- (6) Compton, R. G.; Pilkington, M. B. G.; Stearn, G. M. *J. Chem. Soc., Faraday Trans 1* **1988**, 84, 2155.
- (7) Brookes, B. A.; Ball, J.C.; Compton, R.G. *J. Phys. Chem.*, in press.
- (8) Dryfe, R. A. W. DPhil Thesis, Oxford University, 1995; p 82.
- (9) Bidwell, M. J.; Compton, R. G. *J. Electroanal. Chem. B* **1996**, 417, 119.
- (10) Alden, J. A.; Compton, R. G. *J. Phys. Chem. B* **1997**, 101, 8941.
- (11) Ball, J. C.; Compton, R. G. *J. Phys. Chem. B* **1998**, 102, 3967.
- (12) D02CJF subroutine in the NAG library (Mark 18).
- (13) Thomas, L. H. *Elliptical problems in linear equations over a network*; Watson Sci. Comput. Lab. Rep.; Columbia University: New York, 1949.
- (14) Bruce, G.H.; Peaceman, D.W.; Rachford, H.H.; Rice, J.D. *Trans. Am. Inst. Min. Eng.* **1953**, 198, 79.
- (15) Aoki, K.; Maeda, K. Osteryoung, J. J. *Electroanal. Chem.* **1989**, 272, 17.
- (16) AgraGutierrez, C.; Ball, J.C.; Compton, R.G. *J. Phys. Chem. B* **1998**, 102, 7028.